Springer

Acta Mechanica Sinica

CrossMark click for updates

• RESEARCH PAPER •

Acta Mech. Sin., Vol. 41, 124478 (2025)
https://doi.org/10.1007/s10409-024-24478-x

Atomistic study on the effects of short-range order on the creep behavior of TiVTaNb refractory high-entropy alloy at high temperature

Zhong-Ao Zhang[1], Yan-Kun Dou[1*], Xin-Fu He[1*], Yong-Peng Zhao[1], Wen-Jia Jiang[2], and Wen Yang[1]

[1] *Institute of Reactor Engineering Technology, China Institute of Atomic Energy, Beijing 102413, China;*
[2] *Department of Nuclear Technology and Application, China Institute of Atomic Energy, Beijing 102413, China*

Received August 27, 2024; accepted September 24, 2024; published online January 14, 2025

Creep is an important mechanical property of refractory high-entropy alloys (RHEAs) at high temperatures. The existence of short-range order (SRO) and its ability to improve the strength or plasticity of high-entropy alloys (HEAs) have been experimentally proven. However, there is still little research on the correlation between SRO and creep behavior. The mechanism of SRO influencing creep behavior is not yet clear. In this work, the creep behaviors of TiVTaNb RHEA with and without SRO were simulated at various temperatures and stresses using molecular dynamics methods, and the effects of SRO on creep behavior were analyzed. The results show that the SRO is energetically favorable for occurrence in this RHEA. For polycrystalline RHEAs, grain boundary energy is an important driving force for the formation of SRO. Significantly, under the same conditions, the SRO can reduce the steady-state creep rate and change the creep mechanism of the RHEA. Specifically, the models with SRO will exhibit lower stress exponent and grain-size exponent. A mechanism by which SRO reduces the effects of grain boundaries on creep has been discovered. These phenomena can be well explained by the effects of SRO on atomic diffusion. In addition, by analyzing the diffusion ability of different elements, SRO can induce localization of atomic diffusion, resulting in strain localization under high stresses. This work highlights the importance of SRO on the creep of RHEAs and provides a reference for establishing a reasonable creep model of RHEAs.

Refractory high-entropy alloy, Creep, Short-range order, Molecular dynamics

Citation: Z.-A. Zhang, Y.-K. Dou, X.-F. He, Y.-P. Zhao, W.-J. Jiang, and W. Yang, Atomistic study on the effects of short-range order on the creep behavior of TiVTaNb refractory high-entropy alloy at high temperature, Acta Mech. Sin. 41, 124478 (2025), https://doi.org/10.1007/s10409-024-24478-x

1. Introduction

With the development of nuclear reactor technology, the demand for materials is ever-increasing. In recent years, high-entropy alloys (HEAs) have shown superior performances as a new type of material [1,2]. HEAs usually exhibit higher configurational entropy and different mechanical properties [3]. Refractory high-entropy alloys (RHEAs) have been a kind of promising candidates for high-temperature structural materials for nuclear reactors due to their exceptional properties, including high melting points, excellent strength at elevated temperatures, good corrosion, and radiation resistance [4-9]. TiVTaNb RHEA was first reported by Yang et al. [10] in 2012, which exhibits promising compressive yield strength and ductility at room temperature. Subsequently, Lee et al. [11] and Chen et al. [12] studied the compressive and tensile properties of TiVTaNb RHEA over a wide temperature range, respectively, and found that it has excellent high-temperature stability and strength. Uglov et al. [13,14] discovered the positive irradiation stability of TiVTaNb RHEA through ion irradiation experiments. Yin et al. [15] evaluated the good impact performance of TiVTaNb RHEA. However, the creep be-

*Corresponding authors. E-mail addresses: douyankun@cnncmail.cn (Yan-Kun Dou); hexinfu@cnncmail.cn (Xin-Fu He)
Executive Editor: Zhuhua Zhang

havior of TiVTaNb RHEA and the key influencing factors are still unclear. Because the creep behavior of RHEAs at high temperatures is one of the most crucial factors for ensuring the long-term reliability and safety of nuclear components [16,17], it is worthwhile to study the creep behavior of TiVTaNb RHEA at high temperatures.

In recent years, only a little research on the creep behavior of RHEAs has been reported. Gadelmeier et al. [18] compared the creep properties of HfNbTaTiZr RHEA with a single crystal of Ni-based superalloy CMSX-4 at 1373 K. The solid solution matrix of CMSX-4 had better creep performance than HfNbTaTiZr RHEA. However, it should be noted that CMSX-4 had a much lower melting point of 1603 K, compared to 2210 K for HfNbTaTiZr RHEA. HfNbTaTiZr RHEA has a wider service temperature range. Liu et al. [19] reported the creep behaviors of HfNbTaTiZr RHEA up to 1523 K. The study found the creep behavior was related to the solute drag mechanism. The main impact on the creep rate was the diffusivity of Ta. Compared to the HfNbTaTiZr RHEA and the solid solution matrix of CMSX-4, $Nb_{45}Ta_{25}Ti_{15}Hf_{15}$ RHEA had superior creep resistance, especially at high applied stresses [20]. Cross-kink collisions from screw dislocations controlled the creep deformation in $Nb_{45}Ta_{25}Ti_{15}Hf_{15}$ RHEA at 1173 K.

Due to the limited studies on the creep of RHEAs, their creep mechanism is not yet understood. Depending on the temperature and stress level, several creep mechanisms have been identified in conventional alloys. At low stresses and high temperatures, diffusional creep mechanisms are the main influencing factors, such as Coble creep [21] (diffusion along grain boundaries) and Nabarro-Herring creep [22] (diffusion through the lattice). At higher stresses, dislocation creep mechanisms, such as dislocation glide and climb, become more important [23]. For alloys like Ni-based superalloys with multiphase structures, the effects of multiphase structure on creep have also been widely studied [24,25]. However, compared to conventional alloys, multiple principal elements in RHEAs may lead to different creep behavior [8], especially the impact of short-range order (SRO).

HEAs can exhibit varying degrees of SRO, where specific element pairs tend to cluster or avoid each other. This deviation from a truly random solid solution can significantly impact atomic diffusion, dislocation dynamics, and the mechanical properties of HEAs. Xing et al. [26] simultaneously studied the effects of SRO on diffusion in FCC CrCoNi and BCC MoNbTa. Vacancy-mediated diffusion was suppressed in both HEAs due to the SRO. Yin et al. [27] researched the effects of SRO on the mobilities of dislocations in MoNbTaW RHEA. The SRO was found to induce a temperature-dependent strengthening effect on the screw dislocations moving through the kink-pair nucleation mechanism, which provides extra strengthening for the RHEA. In contrast, Liu and Curtin [28] studied the energy barrier of edge dislocation motion in a binary NbW alloy and demonstrated the decrease in strength caused by SRO. To demonstrate the actual impact of SRO, Moniri et al. [29] determined the 3D atomic positions of HEA nanoparticles for the first time in the experiment and elaborated on the relationship between SRO and heterogeneous strain. Therefore, studying the effects of SRO is crucial for understanding the creep properties of RHEAs.

Atomic scale simulation is an essential tool for revealing microscopic mechanisms. In recent years, molecular dynamics (MD) simulations have been successfully used to study creep in various materials, including nanocrystal metals and alloys, providing detailed information about the underlying mechanisms. Kale et al. [30] investigated the tensile creep resistance of a nanocrystalline Cu-Ta alloy through experiments and simulations. Through atomic scale simulation, the author found that the addition of Ta nanoclusters inhibited the migration of grain boundaries and ultimately led to the unusual tensile creep behavior. Wang et al. [31] investigated the creep mechanisms of nanocrystalline 316L austenitic stainless steels at high temperature. The author discovered different creep mechanisms at different stages of creep. Yao et al. [32,33] investigated the creep behavior of a FeCrAl alloy with different grain sizes over a large temperature and stress range. The transition of the creep mechanism with different stresses was discovered. Huang et al. [34] studied the effects of SRO on the creep behavior of medium-entropy alloy CoCrNi. The author elaborated on the creep behavior of CoCrNi with SRO in detail but did not consider the factor of grain sizes.

This work aims to use MD simulations to provide valuable insights into the atomic-level processes governing the high-temperature deformation of BCC TiVTaNb RHEA and insights into the effects of SRO on the creep deformation of the RHEA. Hybrid MD/MC (Monte Carlo) simulations were used to generate RHEA models with SRO. Creep deformation on the RHEA models with and without SRO was simulated at different temperatures and stresses. The detailed simulation process is described in Sect. 2. The expected results will contribute to the development of improved RHEAs with enhanced creep resistance and be valuable for establishing a reasonable creep model of RHEAs.

2. Methods

Large-scale atomic/molecular massively parallel simulator [35] (LAMMPS) is used for MD simulations. Interatomic interactions were described by the recently developed TiVTaNb Finnis-Sinclair interatomic potential [36], which provides a good description of the alloy's formation en-

thalpy and elastic constants.

To study the effects of SRO on the creep behavior of TiVTaNb RHEA, TiVTaNb models with SRO and without SRO were prepared. Firstly, four Nb models with different grain sizes were generated in Atomsk [37]. Grain boundaries were randomly generated using the Voronoi tessellation method [38] implemented in the Atomsk code. Then by randomly replacing Nb atoms with Ti, V, and Ta atoms, each accounting for 25%, the polycrystalline TiVTaNb RHEA models were constructed. Because of the random distribution of atoms, these models without SRO were named "random models". The hybrid MD/MC simulations were used to generate the SRO in TiVTaNb. Random models were fully relaxed under the isothermal isobaric (NPT) ensemble at 300 K. For every 100 MD steps (timestep = 1 fs), two different type atoms were randomly selected and then swapped 100 times according to the Metropolis Criteria [39]. In total, there were four different grain sizes models with SRO prepared by swapping atoms 7 million named "ordered models". As shown in Fig. 1(a), the potential energy decreased significantly after 7 million swaps, indicating the formation of a more energy-favorable solid solution (as shown in Fig. 1(b)). To quantify the degree of SRO, the Warren-Cowley parameter (WCP) was employed, which can be calculated by [40,41]:

$$WCP_{ij} = 1 - \frac{Z_{ij}}{\chi_i Z_j}, \tag{1}$$

where Z_{ij} is the number of i-type atoms in the first-nearest neighbors of j-type atoms, Z_j is the total number of atoms in the first-nearest neighbors of j-type atoms, and χ_i indicates the atomic fraction of i-type atoms in the RHEA. For completely random multi principal component systems, WCP_{ij} equals 0. A positive WCP_{ij} indicates the i-j pairs separate from each other and cause segregation (short-range clustering), while a negative WCP_{ij} indicates the i-j pairs are favorable and cause SRO.

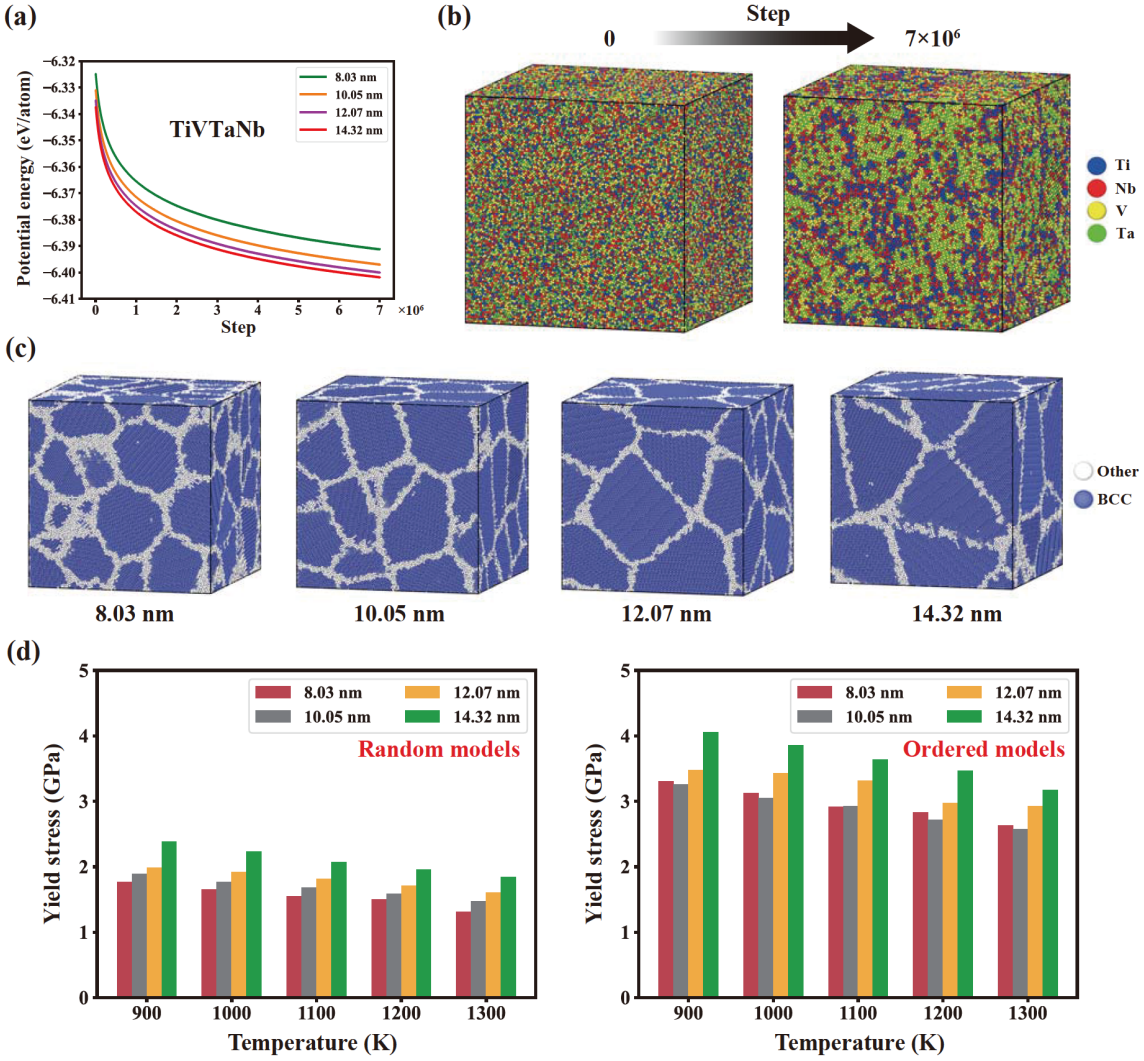

Figure 1 (a) The decrease in potential energy of four TiVTaNb models with different grain sizes during swapping atoms; (b) the atoms configurations equilibrated of 10.05 nm grain size model before and after atomic swap; (c) random models for TiVTaNb samples' highlighted crystal structure type by common neighbor analysis at four grain sizes; (d) the yield stresses of random models and ordered models by tensile simulations.

The size of models was ~24.1 nm × 24.1 nm × 24.1 nm. Figure 1(c) shows the established random models with grain sizes of 8.03, 10.05, 12.07, and 14.32 nm, respectively. The crystal structures of ordered models were same to random models. Table 1 shows the parameters of the models with different grain sizes. To eliminate the residual and thermal stresses, all models were energetically minimized by the conjugate gradient method and equilibrated at desired temperatures and 0 bar under the NPT ensemble for 100 ps.

Due to the need for creep simulations to be conducted during the elastic stage, it was necessary to ensure the yield stresses of the models at different temperatures. According to the results provided by Yao et al. [42], the calculated solidus temperature of TiVTaNb RHEA was 2177 K using JmatPro. The melting point simulated by the interatomic potential in this study using the one-phase method [43] was about 1962 K of random models and 2005 K of ordered models. The two demonstrated good consistency. In addition, the application temperature of TiVTaNb RHEA was expected to be above 873 K. Therefore, the creep simulations in this study were performed at 900, 1000, 1100, 1200, and 1300 K, ranging from 45% to 66% of the melting point. Then, a series of uniaxial tensile simulations were used to calculate the yield stresses at different temperatures. Uniaxial tensile deformation was adopted in the *y*-axis direction with a strain rate of 4×10^{8} s^{-1} for 500 ps (timestep = 1 fs). During the tensile deformation, the NPT ensemble was applied in the *x*-axis and *z*-axis directions to maintain zero lateral pressure. Periodic boundary conditions were applied in all three directions. According to material mechanics, the stress corresponding to 0.2% plastic strain is selected as the yield stress. The tensile simulation results are shown in Fig. 1(d). Due to the contribution of SRO, the strengths of models have significantly improved. The applied stresses were taken lower than the yield stress. Values were taken every 0.1 GPa between 0.5 and 1.2 GPa for random models and every 0.2 GPa between 0.8 and 2.2 GPa for ordered models. For the samples established in this work, these stresses covered most of the range where creep may occur. Then, under different stresses applied along the *y*-axis, the creep simulations were conducted for 2 ns under the NPT ensemble while ensuring that no stress was applied in the other two directions. The atomic-scale deformation mechanisms were analyzed by using common neighbor analysis [44], dislocation analysis [45], and Wigner-Seitz defect analysis, which provided the details of the evolution of microstructure in TiVTaNb RHEA with the cooperation of visualization program-OVITO [46].

3. Results and discussions

3.1 The SRO in TiVTaNb RHEA

The WCPs of different samples are shown in Fig. 2. There is no significant difference in WCPs between models with different grain sizes. Taking the 10.05 nm models as an example, it is found that $WCP_{ij} = 0$ for all random models. There are almost no *i*-*j* pairs orderly distributed within the system. For ordered models, Ti-Ti pairs ($WCP_{\mathrm{TiTi}} = -0.74$), Ti-Nb pairs ($WCP_{\mathrm{TiNb}} = -0.29$), Nb-Nb pairs ($WCP_{\mathrm{NbNb}} = -0.09$), V-V pairs ($WCP_{\mathrm{VV}} = -0.41$), V-Ta pairs ($WCP_{\mathrm{VTa}} = -0.45$) and Ta-Ta pairs ($WCP_{\mathrm{TaTa}} = -0.16$) exhibit preference, while other atomic pairs separate from each other. Furthermore, the distribution of elements in grain boundaries and grain interiors was statistically analyzed for ordered models, as shown in Fig. 3. The proportion of each element in grain boundaries or grain interiors is around 25% for random models, which is consistent with the definition of the random model. However, there is a significant difference in the distribution of elements in grain boundaries and grain interiors for ordered models. The proportion of Ti atoms (≈ 45%) and Nb atoms (≈ 30%) in grain boundaries is significantly higher, while the proportion of V atoms (≈ 27%) and Ta atoms (≈ 30%) in grain interiors is dominant. A comparison of the structure and element distribution of the 10.05 nm ordered model in Fig. 3(e) can provide a more intuitive view of the phenomenon. It is found that SRO in TiVTaNb RHEA tends to have two distributions. Ti-Ti/Ti-Nb/Nb-Nb pairs tend to cluster in grain boundaries, while V-V/V-Ta/Ta-Ta pairs tend to combine in grain interiors. Similar phenomena have also been found in the studies of Li et al. [47] and Chen et al. [41]. Li et al. [47] found that Nb atoms tended to segregate to the grain boundaries, accompanied by enrichment of W atoms in grain interiors in NbMoTaW RHEA. In addition, Li et al. [47] indicated that this effect can be explained by the grain boundary energies.

Table 1 Parameters of TiVTaNb models

	Grain size (nm)	Number of grains	Number of atoms	Fraction of grain boundary atoms (%)
Random models	8.03	51	820429	31.11
	10.05	26	820468	24.69
	12.07	15	820318	20.68
	14.32	9	820439	18.25
Ordered models	8.03	51	820429	29.31
	10.05	26	820468	23.26
	12.07	15	820318	19.69
	14.32	9	820439	17.09

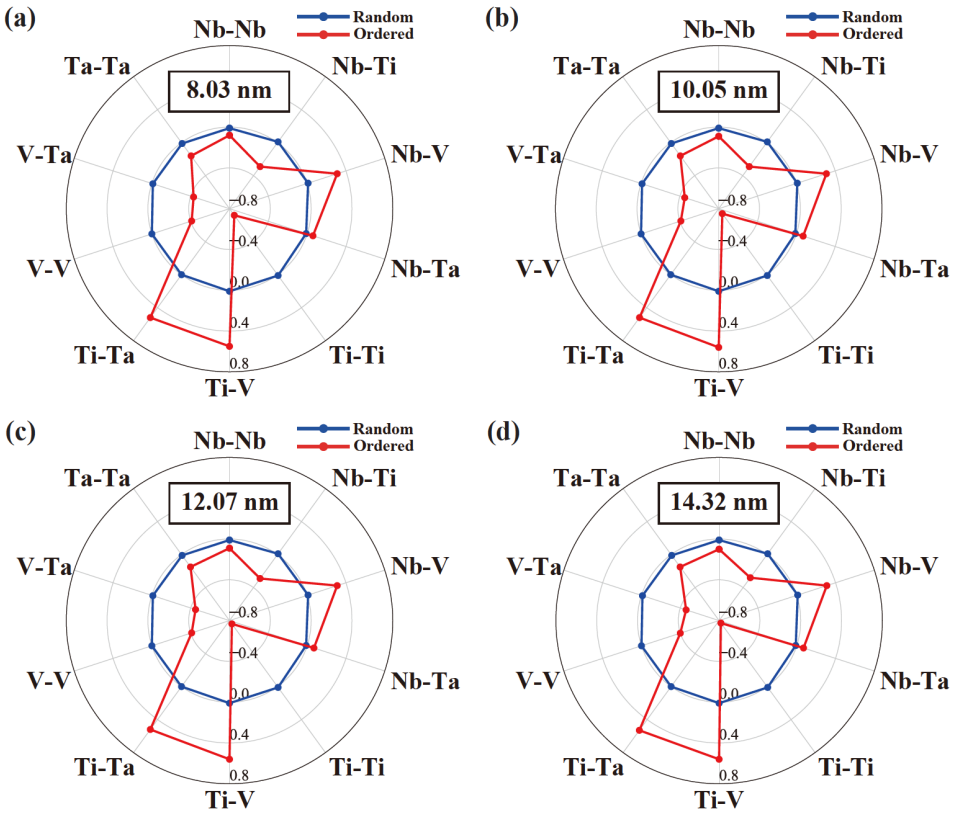

Figure 2 Corresponding WCP of different samples with grain sizes of (a) 8.03, (b) 10.05, (c) 12.07, and (d) 14.32 nm.

Chen et al. [41] found that Ti-neighboring pairs and Mo-/Zr-neighboring pairs were formed in grain boundaries of MoTaTiWZr RHEA. The author still studied the differences in chemical affinity (normalized cohesive energies) between elements and found that low-energy clusters (strong chemical affinity) formed only in grain interiors.

To explain the formation of SRO in TiVTaNb RHEA, cohesive energies (as shown in Table 2) and grain boundary energies (as shown in Fig. 4) were calculated. The consistency with experimental values and density functional theory (DFT) demonstrates the applicability of the Finnis-Sinclair interatomic potential. Beyond expectation, the simulation results failed to reflect the differences in chemical affinity between grain boundaries and grain interiors. For example, Nb-Nb pairs with strong chemical affinity also formed in grain boundaries. However, the differences in grain boundary energies can effectively explain the formation of SRO in TiVTaNb RHEA. Ti and Nb have relatively low grain boundary energies, while Ta and V have relatively high grain boundary energies among the four component elements. Therefore, Ti and Nb segregation to the grain boundaries and Ta and V enrichment in grain interiors are driven by a thermodynamic driving force to lower the grain boundary energies. The formation of SRO in polycrystalline materials is controlled by intrinsic factors of grain boundary energies. The issue of unclear differences in chemical affinity in this study may be caused by the differences in grain boundaries. Compared to Ref. [41], the proportion of grain boundaries simulated in this study is larger. The role of grain boundaries is more significant. Chemical affinity will not be able to explain the variation of SRO by grain boundaries. Shi et al. [48] reported the differences in Cr segregation behavior between the bulk and grain boundaries. Therefore, the grain boundary is an important factor affecting SRO in polycrystalline systems, especially nanocrystals.

3.2 Effects of SRO on the creep behavior

The steady-state creep rate is an important physical quantity describing creep, implying that the system reaches the steady-state stage. In this work, when the steady-state creep rate was below 10^{-8} ps^{-1}, there was basically no deformation during creep. As shown by the cold tone curve in Fig. 5(e), the creep of ordered models is not significant at 900 and 1000 K (steady-state creep rate < 10^{-8} ps^{-1}), so it will not be discussed in subsequent discussions. For the convenience of comparison, the steady-state creep rates of all samples at 1100-1300 K are shown in Fig. 5(g) and (h).

The effects of applied stresses, temperature, and grain sizes on the creep behavior of different samples are shown in Fig. 5(a)-(f). From Fig. 5(a) and (d), it can be observed

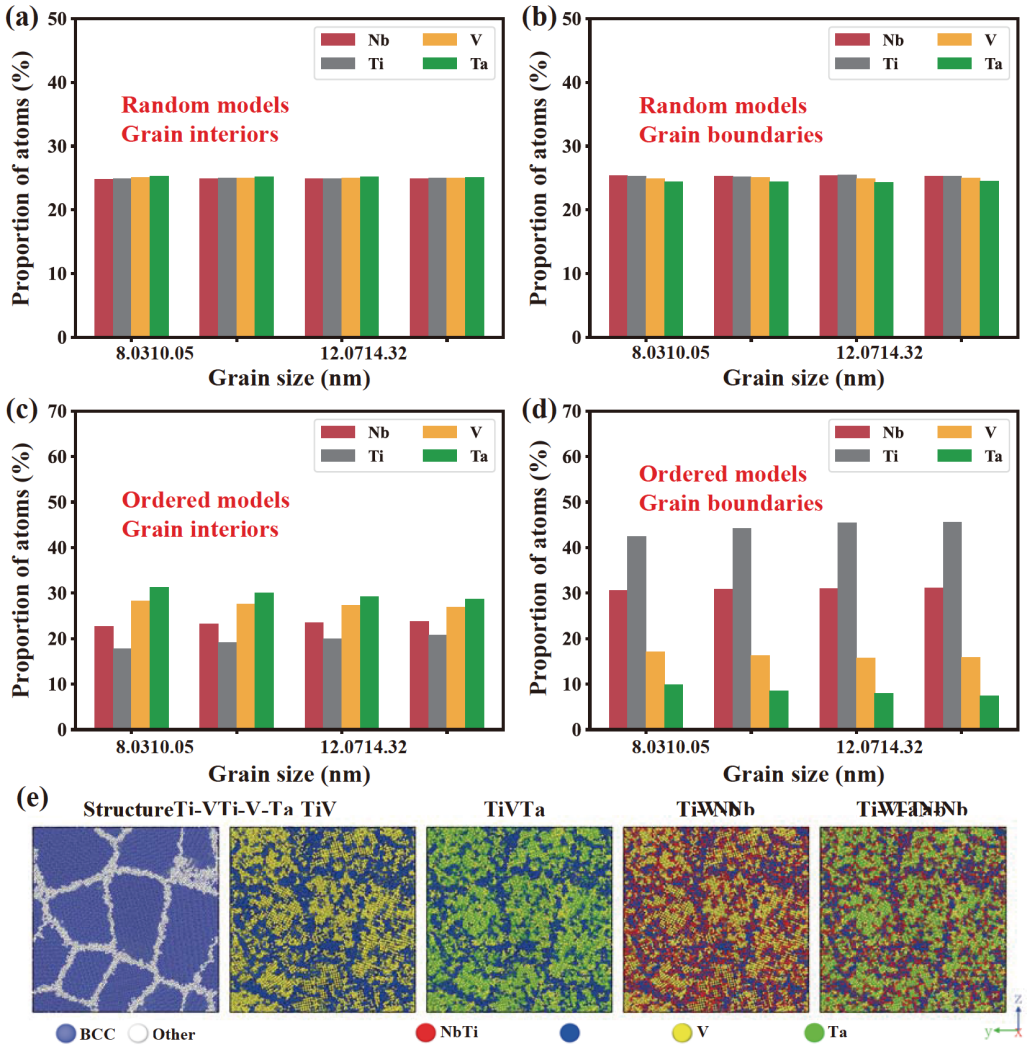

Figure 3 Proportion of atoms (a) in grain interiors of random models; (b) in grain boundaries of random models; (c) in grain interiors of ordered models; (d) in grain boundaries of ordered models; (e) atomic snapshots of the structure and element distribution of the 10.05 nm ordered model.

Table 2 Cohesive energy of *i*-*j* pairs calculated using the potential and compared with experimental values (Exp.) and DFT; the chemical affinity of *i*-*j* pairs calculated using normalized cohesive energy

i-*j* pairs	Cohesive energy (eV)	Exp. [49] (eV)	DFT (eV)	Chemical affinity
Nb-Nb	−7.57	−7.47	−6.94	0.84
Nb-Ti	−6.13	–	−6.17	0.39
Nb-V	−6.38	–	−6.09	0.47
Nb-Ta	−7.84	–	−7.69	0.92
Ti-Ti	−4.85	–	−5.47	0
Ti-V	−5.01	–	−5.26	0.05
Ti-Ta	−6.41	–	−6.83	0.48
V-V	−5.31	−5.3	−5.34	0.14
V-Ta	−6.67	–	−6.76	0.56
Ta-Ta	−8.01	−8.09	−8.44	1

that whether it is a random model or an ordered model, the steady-state creep rate always increases with the increase of applied stresses under the same grain size and temperature. Applied high stresses work on the system, making it easier for dislocations to overcome the energy barrier of obstacles, thereby accelerating plastic deformation. Similarly, with the temperature increase, the steady-state creep rate also shows the same trend, as shown in Fig. 5(b) and (e). This is because the increase in temperature accelerates the thermal activation processes such as point defect diffusion, dis-

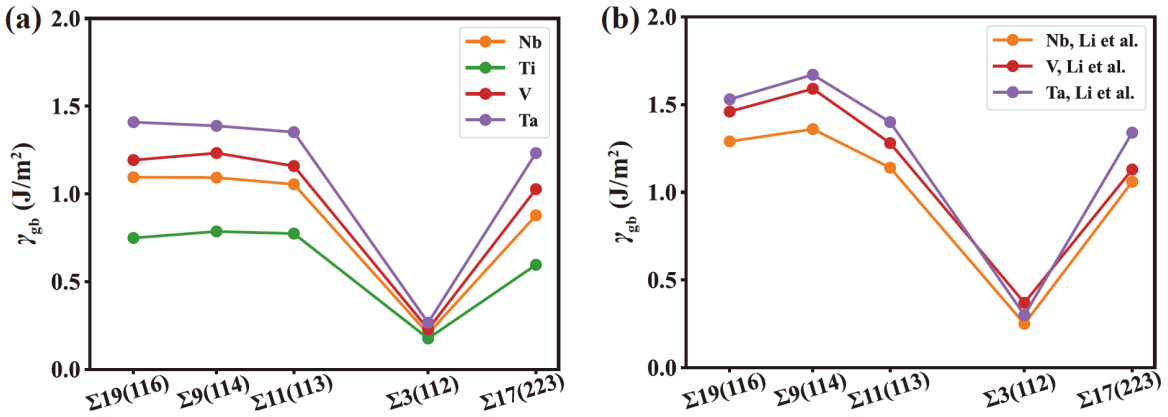

Figure 4 (a) Comparison of partial grain boundary energies between different elements; (b) the grain boundary energies calculated by Li et al. [50] using DFT.

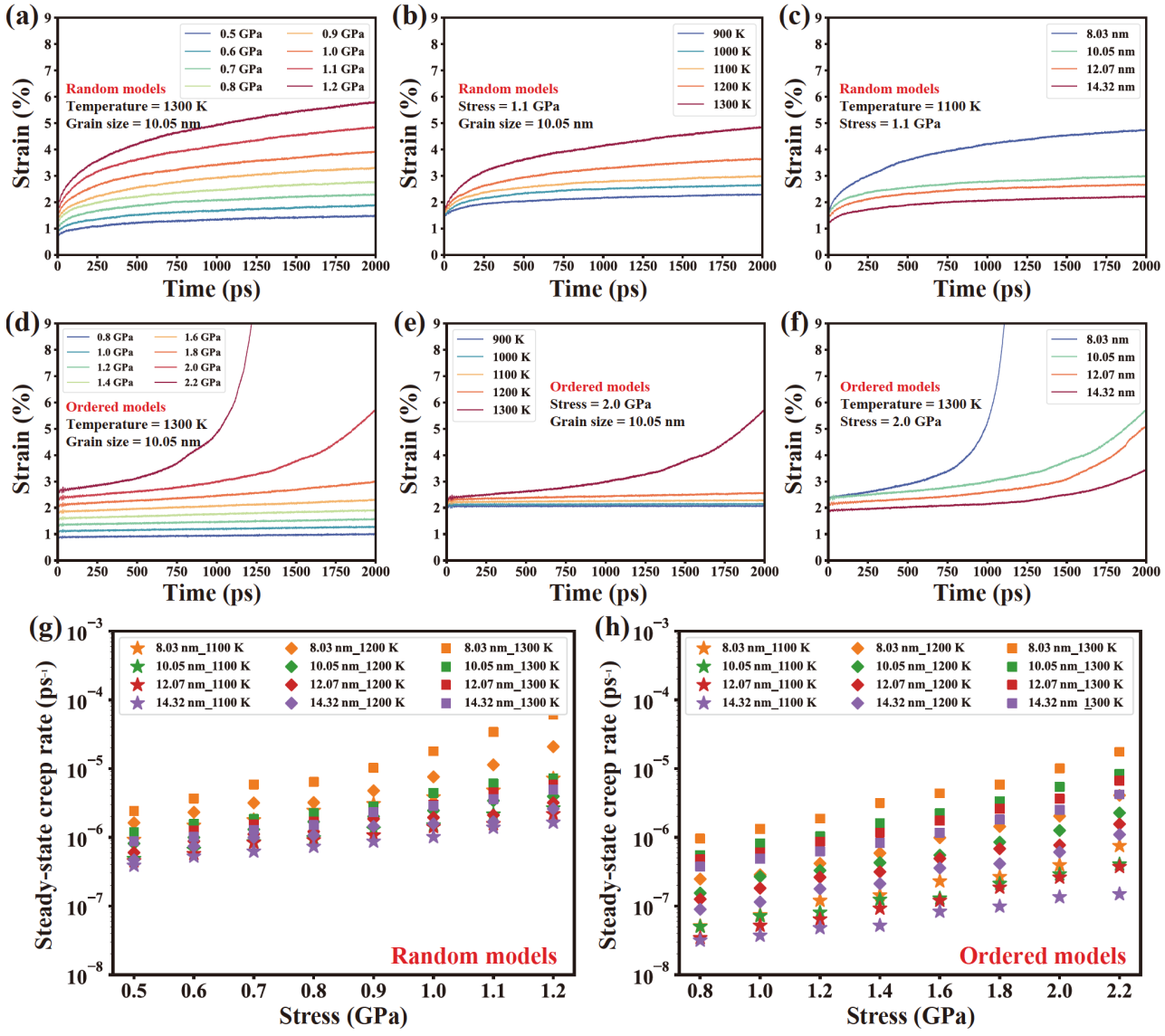

Figure 5 Creep curves of (a) 10.05 nm random models at 1300 K under different stress, (b) 10.05 nm random models under 1.1 GPa at different temperatures, (c) random models under 1.1 GPa at 1100 K with different grain sizes, (d) 10.05 nm ordered models at 1300 K under different stress, (e) 10.05 nm ordered models under 2.0 GPa at different temperature, (f) ordered models under 2.0 GPa at 1300 K with different grain sizes; the steady-state creep rate of (g) random models and (h) ordered models at 1100-1300 K.

location slip and climb, resulting in an increase in steady-state creep rate. The same trend of steady-state creep rate with stresses and temperature is also reflected in creep experiments of other RHEA [19]. Moreover, the variation of steady-state creep rate with grain sizes is shown in Fig. 5(c) and (f). Unlike the variation trend of applied stresses and temperature, the steady-state creep rate decreases with the increase of grain sizes. The creep experiments studied by Shen et al. [51,52] on VNbMoTaW RHEA also found the similar phenomenon. Previous researches indicated that defects formed in grain boundaries as sinks and sources of the lattice dislocations moving in grain interiors caused the plastic flow in nanocrystalline materials [53,54]. Therefore, the decrease in the fraction of grain boundaries slows the diffusion of unstable defects in grain boundaries and restricts dislocation movement, resulting in a lower steady-state creep rate. The above phenomena are consistent with conventional alloys [55].

In order to study the effects of SRO on RHEA creep, the changes of WCP during creep were recorded firstly, as shown in Fig. 6. Figure 6(a) and (b) shows the WCP before and after creep of the 10.05 nm ordered model at 1300 K under applied stress of 1.2 and 2 GPa, respectively. The ordered model reached the steady-state creep stage under 1.2 GPa, and the ordered model reached the tertiary stage under 2 GPa. The blue line represents the WCP of the initial configuration (the same as the red line in Fig. 2(b)), and the red line represents the WCP after creep. It can be observed that regardless of whether it reached the tertiary stage or not, there was no significant change in SRO during creep, indicating that SRO had not been destroyed during creep. Then, the creep curves under the same stress were selected for comparison. Due to the difference in tensile strength between random and ordered models, only 0.8, 1.0, and 1.2 GPa of the same stress were applied to the selected stresses. Figure 7(a) shows the effects of SRO on creep under different stresses. Similarly, Fig. 7(b) and (c) shows different temperatures and grain sizes, respectively. It can be observed that the steady-state creep rate of random models is much higher than that of ordered models under the same

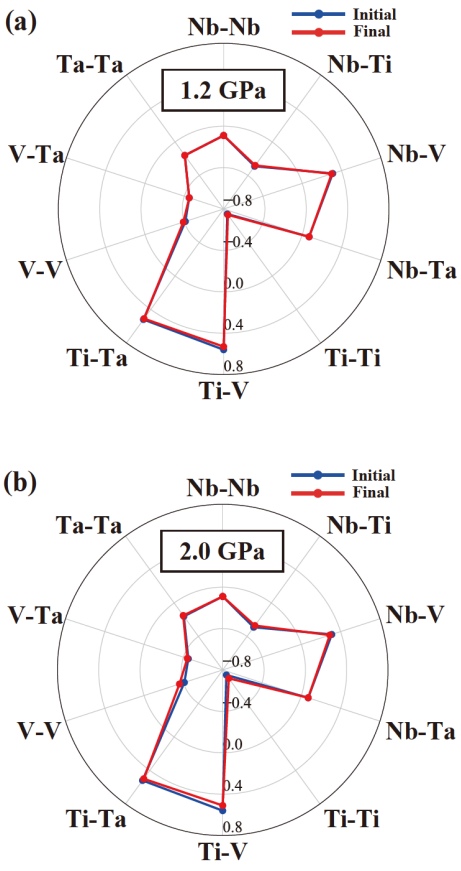

Figure 6 WCP before and after creep of the 10.05 nm ordered model at 1300 K under stress of (a) 1.2 GPa and (b) 2 GPa.

conditions, similar to the results shown in Fig. 5(g) and (h). The applied stresses, temperature, and grain sizes have less influence on the creep rate of ordered models than random models. Therefore, SRO can significantly reduce the steady-state creep rate of TiVTaNb RHEA under the same conditions.

3.3 Effects of SRO on the creep mechanisms

The effects of SRO on creep mechanism are also important to understanding RHEA creep behavior. To characterize the

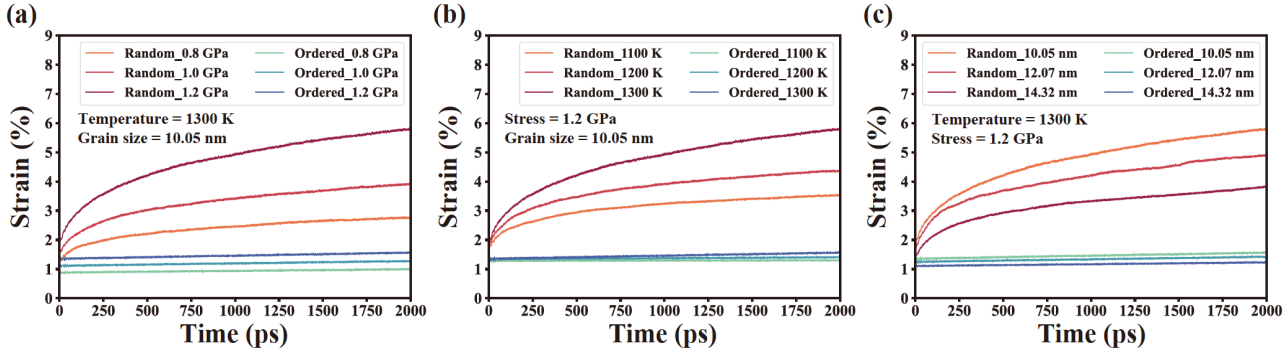

Figure 7 Creep curve of (a) 10.05 nm models with and without SRO at 1300 K, (b) 10.05 nm models with and without SRO under 1.2 GPa, (c) 10.05, 12.07 and 14.32 nm models with and without SRO under 1.2 GPa at 1300 K.

creep mechanism, the known empirical equation was applied to correlate the creep temperature T, stress σ, and grain size d to the creep rate $\dot{\varepsilon}$ [56]:

$$\dot{\varepsilon} = \frac{AD_0Gb}{k_BT}\left(\frac{b}{a}\right)^p\left(\frac{\sigma}{G}\right)^n \exp\left(-\frac{Q_c}{k_BT}\right), \tag{2}$$

where b, G, D_0, A and k_B are Burgers vector, shear modulus (GPa), atomic diffusion coefficient ($m^2 \cdot s^{-1}$), temperature-based constant and Boltzmann's constant, respectively. Referring to Eq. (2), n and p define the stress exponent and grain-size exponent as follows:

$$n = \frac{\partial \log \dot{\varepsilon}}{\partial \log \sigma}, \tag{3}$$

$$p = \frac{\partial \log \dot{\varepsilon}}{\partial \log d}. \tag{4}$$

According to previous study, the values of exponents (n, p) are indicative of dominant mechanism in the creep [56]. The stress exponent $n \approx 1$ indicates that when $p \approx 2$, the creep mechanism is dominated by lattice diffusion [57], and when $p \approx 3$, the creep mechanism is dominated by grain boundary diffusion [21]. If the stress exponent $n \approx 2$, grain boundary sliding becomes the main creep mechanism [58,59]. In addition, the creep mechanism is considered to be dislocation motion, which occurs through dislocation slip and dislocation climb when the stress exponent $n \geq 3$ [23,60].

According to Eqs. (3) and (4), Fig. 8 shows the effects of SRO on the stress exponent n and grain-size exponent p under different conditions. The warm tone curve represents a random model, while the cool tone curve represents an ordered model. For the calculation of stress exponent n, the above three stresses were also selected. As shown in Fig. 8 (a) and (c), the 10.05 nm random models have n = 2.19-3.07 at different temperatures, while the ordered models have n = 1.18-1.89. The random models with different grain sizes have n = 2.8-5.62 at 1300 K, while ordered models have n = 1.27-1.65. It can be found that SRO significantly reduces the stress exponent n. Models can produce smaller deformation under the same stress increment, indicating an enhanced ability of the alloys to resist deformation. This is consistent with the conclusion that SRO reduces the steady-state creep rate. As shown in Fig. 8(b) and (d), p undergoes a transition in the 8.03 nm random models, but the ordered models do not exhibit such a phenomenon. For 8.03 nm models, SRO reduces grain-size exponent p. According to Eq. (2), a decrease in p indicates a reduction of the influence of grain boundaries on creep. From this, it can be inferred that for systems with smaller grain sizes, due to the large proportion of grain boundaries, grain boundaries often have a significant impact on creep, and SRO can reduce the effects of grain boundaries on creep.

According to the previously mentioned theory, considering the values of exponents (n, p) comprehensively, the effects of SRO on the creep mechanism can be obtained. Under the same loading conditions, SRO can change the creep mechanism dominated by grain boundary sliding, or dislocation slip and climb in random models into the creep mechanism dominated by atomic diffusion in ordered models. The changes shown in Fig. 8 during creep fully confirm this viewpoint. Taking the creep simulation of 10.05 nm models at 1200 K with applied stress of 1.2 GPa as an example, under the effects of SRO, the creep mechanism changes from grain boundary slip (n = 2.19) to lattice diffusion (n = 1.75; p = 1.43). The red atoms in Fig. 9 (a), (b), (d) and (e) are reference atoms. Marking red atoms in the initial configuration and tracking the positional changes of these atoms during creep simulation can effectively identify microscopic mechanisms. By comparing Fig. 9(a) and (b), it can be found that red atoms moved along grain boundaries. The random model undergoes significant grain boundary slip after creep, while the ordered model shown in Fig. 9(d) and (e) does not exhibit such a phenomenon. The atomic displacement of the random model shown in Fig. 9(c) after 2000 ps creep further proves that large displacements often exist in grain boundaries. In contrast, the ordered model demonstrated by Fig. 9(f) exhibits lower atomic displacement and more uniform displacement distribution after creep. This simultaneously demonstrates that SRO enhances overall deformation resistance while significantly reducing the impact of grain boundaries on deformation.

In fact, the transition of the creep mechanism due to SRO can be well understood through its strengthening effect. As mentioned earlier, the alloy mainly exhibits diffusion creep at high temperatures and low stresses, while it transforms to grain boundary slip or dislocation climb dominant at high temperatures and high stresses. Therefore, SRO increased the tensile strength of the system (Fig. 1(d)), resulting in high stresses in random models and low stresses in ordered models for the same stresses. This variation in stress level has caused a change in the creep mechanism.

3.4 The correlation between creep and atomic diffusion considering SRO

In summary, the formation of SRO changed the creep mechanism and significantly reduced the creep rate under the same conditions. Given the significant impact of grain boundary energies on the formation of SRO, regulating the grain boundary energy of the system can serve as an indirect approach to enhancing creep resistance. However, the mechanisms by which SRO affects creep behavior are still unclear. As is well known, creep behavior at high temperatures is related to atomic diffusion, grain boundary slip, and dislocation motion. During the steady-state creep stage, which is the focus of this work, the dislocation density remains largely unchanged. It is difficult to draw effective

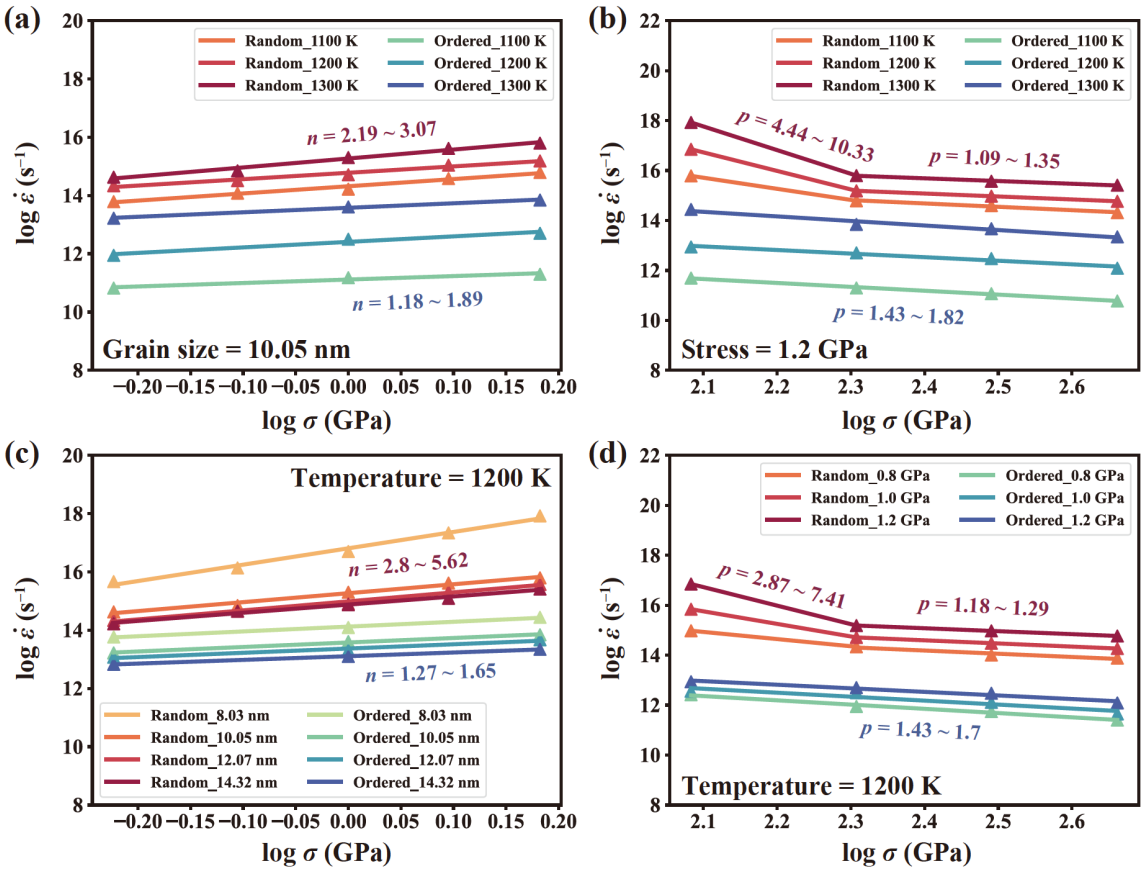

Figure 8 Change of (a) the stress exponent n and (b) the grain-size exponent p caused by SRO at different temperatures; (c) the change of the stress exponent n caused by SRO with different grain sizes; (d) the change of the grain-size exponent p caused by SRO under different stresses.

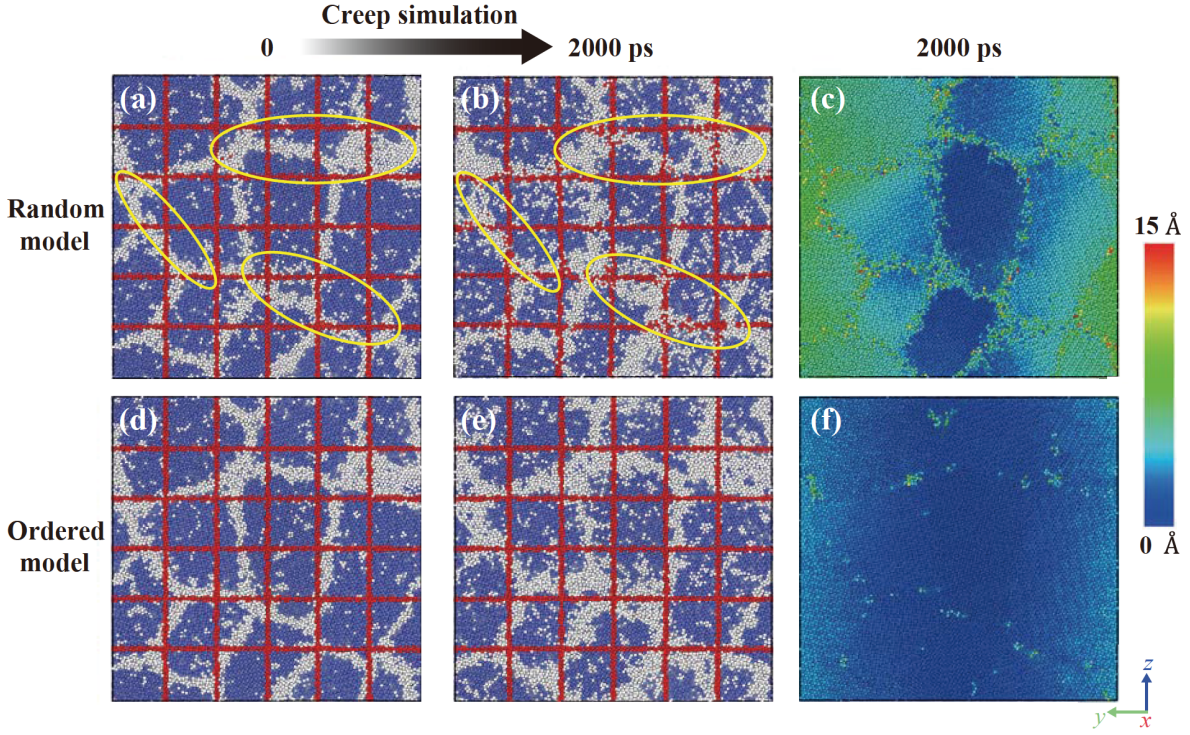

Figure 9 Initial structure (a) with and (d) without SRO; the final structure after creep (b) with and (e) without SRO; atomic displacement after creep (c) with and (f) without SRO.

conclusions from the evolution of dislocations. As mentioned earlier, the influence of grain boundaries can be reflected through atomic motion at the atomic scale. Therefore, to explain the effects of SRO on creep, the atomic diffusion behavior is considered. The diffusion coefficient D is an important parameter that describes the atomic diffusion ability, which is computed with Eq. (5):

$$D = \frac{1}{6}\frac{\mathrm{d}MSD}{\mathrm{d}t}, \tag{5}$$

where t is the time duration. MSD (mean square displacement) can be calculated by Eq. (6) [32,61]:

$$MSD = \left\langle r^2(t) \right\rangle = \left\langle \frac{1}{N}\sum_{i=0}^{N}\left[r_i(t) - r_i(0)\right]^2 \right\rangle, \tag{6}$$

where N is the total number of atoms, and $r_i(0)$ and $r_i(t)$ are the positions of an atom at the initial and current moments, respectively. The D calculated through this method can fully describe the motion of atoms during creep.

Based on previous discussions, SRO seriously affects the grain boundary effects on creep. This has inspired us to explore the differences between grain boundaries and interiors during creep. Therefore, taking the creep of 10.05 nm models at 1100-1300 K under 1.2 GPa as an example, the diffusion coefficients of all atoms (D_{ALL}), atoms in grain boundaries (D_{GB}) and atoms in grain interiors (D_{GI}) were statistically analyzed. As shown in Fig. 10(a)-(c), the diffusion coefficient of ordered models is much smaller than that of random models at any temperature. SRO significantly inhibits atomic diffusion during creep. Figure 11 shows the diffusion paths of some atoms of 10.05 nm models under 1.2 GPa at 1200 K during creep. It can be observed that the introduced SRO shrinks the range of migration trajectory in this system. The diffusion of each element is suppressed in ordered models. This also confirms the small atomic displacement in Fig. 8(c) and (f). In addition, a new normalized parameter D_{p} was defined here to quantify the proportion of atomic diffusion in grain boundaries to the total atomic diffusion in order to determine the contribution of grain boundaries:

$$D_{\mathrm{p}} = \frac{D_{\mathrm{ALL}} - D_{\mathrm{GI}}}{D_{\mathrm{GB}} - D_{\mathrm{GI}}}. \tag{7}$$

The larger the D_{p}, the greater the contribution of grain boundaries. As shown in Fig. 10(d), compared to the random models, the ordered models have a significant decrease in D_{p}. The formation of SRO not only seriously hinders the diffusion of atoms but also changes the contribution level of different regions. This is consistent with the transition of the creep mechanisms discussed in Sect. 3.3.

From Fig. 10(b) and (c), it can also be found that although

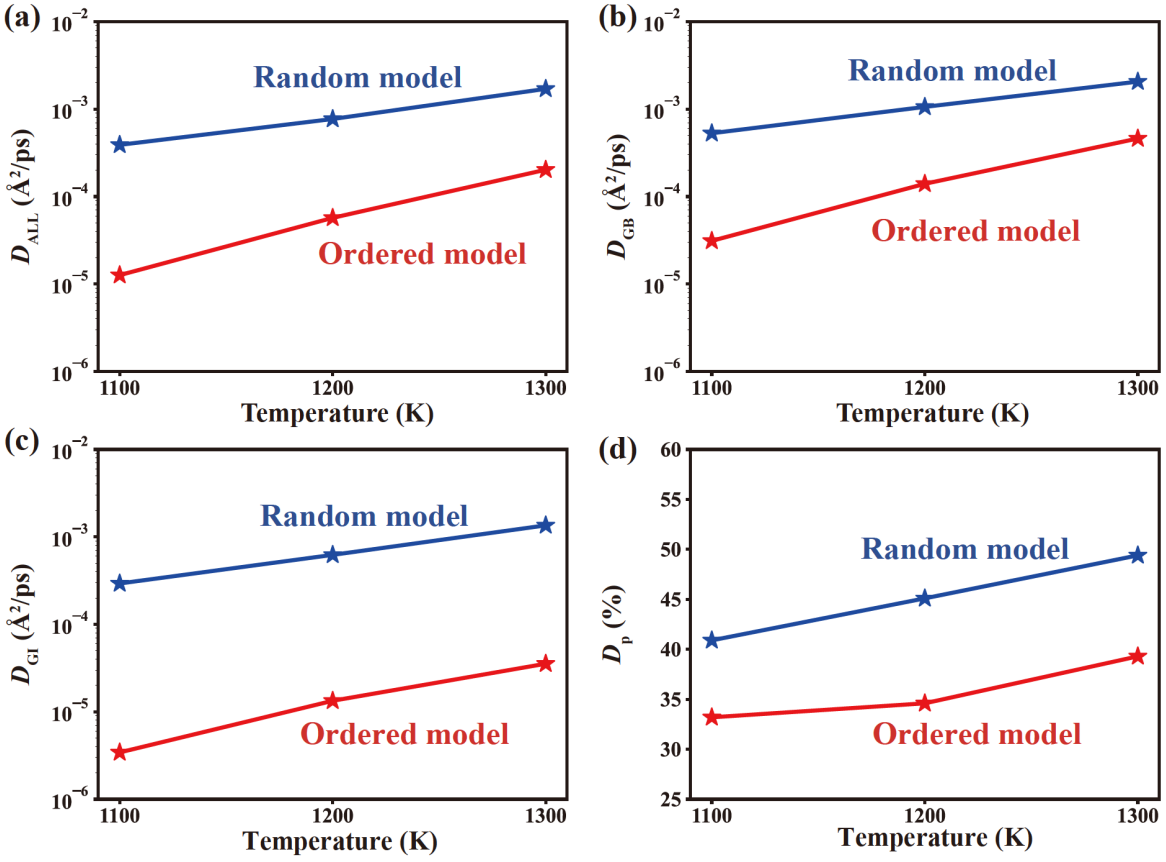

Figure 10 Diffusion coefficients of (a) all atoms, (b) atoms in grain boundaries, and (c) atoms in grain interiors with 10.05 nm models at different temperatures; (d) the normalized parameter D_{p} of 10.05 nm models at different temperatures.

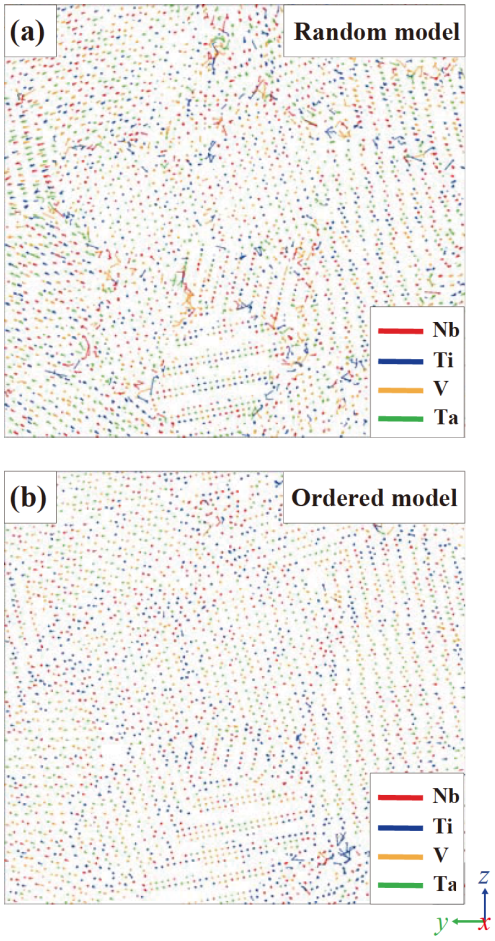

Figure 11 Diffusion paths of some atoms of 10.05 nm models (a) with and (b) without SRO under 1.2 GPa at 1200 K.

the diffusion coefficients in grain boundaries and grain interiors decrease, the degree of reduction varies. In ordered models, the diffusion coefficients of atoms in grain boundary are on the order of 10^{-4}, while the diffusion coefficients of atoms in grain interiors are only on the order of 10^{-5}. To understand this difference, taking the results at 1300 K as an example, the diffusion coefficients of each element were extracted, as shown in Fig. 12(a). The diffusion coefficients of each element in random models are not significantly different, with D_{Ti} and D_V slightly higher. The difference in diffusion coefficients in ordered models is amplified. D_{Ti} is significantly the highest, while D_{Ta} is the lowest, and D_{Nb} is slightly higher than D_V. This difference coincides with SRO. Ti atoms and Nb atoms enriched in grain boundaries have stronger diffusion ability, while V atoms and Ta atoms enriched in grain interiors are "less likely to move". The phenomenon of reduced and localization diffusion caused by SRO also occurred in the study of Xing et al. [26]. Xing et al. [26] found that the diffusion coefficients of all components decreased to varying degrees, with Ta having the greatest decrease in the presence of SRO in NbMoTa RHEA. Due to the presence of SRO, an increase in migration barrier and an enhanced diffusion correlation leads to a decrease in diffusivity. It is worth noting that this localized diffusion is likely to develop into strain localization under high stresses. Figure 12(b) shows the shear strain of the 10.05 nm ordered model after creep under 1.6 GPa at 1200 K. It can be observed that the high strain zone highly overlaps with the Ti and Nb rich zones.

Through the above discussion, the effects of SRO on atomic diffusion are consistent with the effects on creep. The impact of SRO on atomic diffusion behavior is reflected in the macroscopic performance of reduction of creep rate and changes in deformation.

4. Conclusion

In this work, the effects of SRO on the creep performance of TiVTaNb RHEA at high temperatures were studied using MD simulations. Through the analysis of SRO, steady-state creep rate and creep mechanism of different samples, the following conclusions can be drawn:

(1) For polycrystalline systems, especially nanocrystals (large proportion of grain boundaries), the grain boundary energy of component elements in RHEA has an impact on the formation of SRO. Given the effects of SRO on creep, regulating the grain boundary energy of the system may serve as an indirect approach to enhancing creep resistance.

(2) SRO seriously affects RHEA's creep behavior. It leads to a decrease in steady-state creep rate and a transition of the

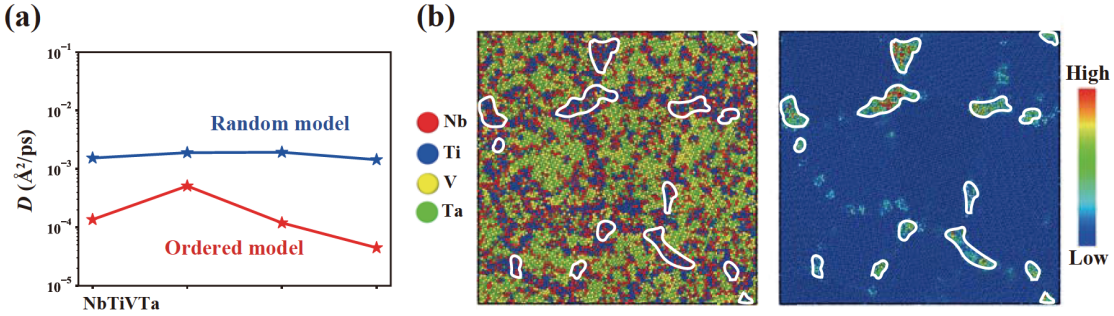

Figure 12 (a) Diffusion coefficients of different elements of 10.05 nm models with and without SRO under 1.2 GPa at 1300 K; (b) atomic snapshot and shear strain after creep of the 10.05 nm model under 1.6 GPa at 1200 K.

creep mechanisms under the same loading conditions. SRO weakens the effects of grain boundaries on creep and leads to strain localization under high stresses.

(3) The effects of SRO on atomic diffusion and creep behavior are highly consistent. The presence of SRO significantly hinders atomic diffusion and reduces its effects in grain boundaries. The formation of SRO can also lead to significant differences in the diffusion ability of different elements. The enrichment zones, containing elements with high diffusion coefficients, will experience significant deformation, leading to an uneven distribution of strain.

This work focuses on the specific effects of SRO on creep. Reasonable regulation of SRO can enhance the creep performance of RHEA. This work also provides a valuable reference for developing a reliable creep model for RHEA, enabling accurate predictions of RHEA's creep behavior.

Conflict of interest *On behalf of all authors, the corresponding author states that there is no conflict of interest.*

Author contributions ***Zhong-Ao Zhang:*** *Conceptualization, Methodology, Software, Formal analysis, Investigation, Data Curation, Writing – Original Draft, Writing – Review & Editing, Visualization.* ***Yan-Kun Dou:*** *Conceptualization, Methodology, Validation, Investigation, Resources, Writing – Review & Editing, Supervision, Project administration, Funding acquisition.* ***Xin-Fu He:*** *Resources, Writing – Review & Editing, Supervision, Funding acquisition.* ***Yong-Peng Zhao:*** *Investigation, Methodology, Funding acquisition.* ***Wen-Jia Jiang:*** *Writing – Original Draft, Writing – Review & Editing.* ***Wen Yang:*** *Resources, Writing – Review & Editing, Supervision, Funding acquisition.*

Acknowledgements *This work was supported by the National Natural Science Foundation of China (Grant No. 12405324), the CNNC Science Fund for Talented Young Scholars, the Dean's Fund of China Institute of Atomic Energy (Grant No. 219256), and the Director's Fund of China Institute of Atomic Energy (Grant No. 218296).*

1 J. Yeh, S. Chen, S. Lin, J. Gan, T. Chin, T. Shun, C. Tsau, and S. Chang, Nanostructured high-entropy alloys with multiple principal elements: Novel alloy design concepts and outcomes, Adv. Eng. Mater. **6**, 299 (2004).
2 E. P. George, D. Raabe, and R. O. Ritchie, High-entropy alloys, Nat. Rev. Mater. **4**, 515 (2019).
3 M. Ren, B. Li, and H. Fu, Formation condition of solid solution type high-entropy alloy, Trans. Nonferrous Met. Soc. China **23**, 991 (2013).
4 O. N. Senkov, G. B. Wilks, J. M. Scott, and D. B. Miracle, Mechanical properties of $Nb_{25}Mo_{25}Ta_{25}W_{25}$ and $V_{20}Nb_{20}Mo_{20}Ta_{20}W_{20}$ refractory high entropy alloys, Intermetallics **19**, 698 (2011).
5 D. B. Miracle, and O. N. Senkov, A critical review of high entropy alloys and related concepts, Acta Mater. **122**, 448 (2017).
6 O. El Atwani, H. T. Vo, M. A. Tunes, C. Lee, A. Alvarado, N. Krienke, J. D. Poplawsky, A. A. Kohnert, J. Gigax, W. Y. Chen, M. Li, Y. Q. Wang, J. S. Wróbel, D. Nguyen-Manh, J. K. S. Baldwin, O. U. Tukac, E. Aydogan, S. Fensin, and E. Martinez, Author correction: A quinary WTaCrVHf nanocrystalline refractory high-entropy alloy withholding extreme irradiation environments, Nat. Commun. **14**, 3490 (2023).
7 M. A. Tunes, S. Fritze, B. Osinger, P. Willenshofer, A. M. Alvarado, E. Martinez, A. S. Menon, P. Ström, G. Greaves, E. Lewin, U. Jansson, S. Pogatscher, T. A. Saleh, V. M. Vishnyakov, and O. El-Atwani, From high-entropy alloys to high-entropy ceramics: The radiation-resistant highly concentrated refractory carbide (CrNbTaTiW)C, Acta Mater. **250**, 118856 (2023).
8 O. N. Senkov, D. B. Miracle, K. J. Chaput, and J. P. Couzinie, Development and exploration of refractory high entropy alloys—A review, J. Mater. Res. **33**, 3092 (2018).
9 D. B. Miracle, High entropy alloys as a bold step forward in alloy development, Nat. Commun. **10**, 1805 (2019).
10 X. Yang, Y. Zhang, and P. K. Liaw, Microstructure and compressive properties of NbTiVTaAlx high entropy alloys, Procedia Eng. **36**, 292 (2012).
11 C. Lee, D. Xie, J. Li, A. Huang, C. Lear, E. Mirkoohi, B. Prorok, M. Meyers, H. Xu, G. Song, P. Liaw, G. Gray, N. Li, and S. Fensin, Dynamic deformation behaviors in single body-centered-cubic (BCC) phase refractory high-entropy alloys, doi: 10.21203/rs.3.rs-3471175/v1.
12 J. Chen, Y. Dong, K. Jin, B. Wang, and Y. Xue, Homogenization of TiVTaNb refractory high-entropy alloy, J. Phys.-Conf. Ser. **2383**, 012136 (2022).
13 V. V. Uglov, S. V. Zlotsky, M. M. Belov, A. E. Ryskulov, I. A. Ivanov, A. E. Kurakhmedov, D. A. Mustafin, A. D. Sapar, and K. Jin, Structural and phase states on concentrated solid solution of the V-Nb-Ta-Ti system irradiated by krypton ions, J. Belarusian State Univ. Phys. **1**, 14 (2023).
14 V. V. Uglov, S. V. Zlotski, M. M. Belov, A. E. Ryskulov, K. Jin, I. A. Ivanov, A. E. Kurakhmedov, D. A. Mustafin, A. D. Sapar, and Y. V. Bikhert, Structural and phase changes in concentrated V-Nb-Ta-Ti solid solutions irradiated by helium ions, J. Surf. Investig. **17**, 208 (2023).
15 X. Yin, Y. K. Dou, X. F. He, K. Jin, C. L. Wang, Y. G. Dong, C. Y. Wang, Y. F. Xue, and W. Yang, Effects of Nb addition on Charpy impact properties of TiVTa refractory high-entropy alloy, Acta Metall. Sin. (Engl. Lett.) **36**, 405 (2023).
16 K. S. Chan, The constitutive representation of high-temperature creep damage, Int. J. Plast. **4**, 355 (1988).
17 D. W. A. Rees, and B. F. Dyson, Deformation and fracture behaviour under combined creep and fatigue, Int. J. Plast. **2**, 1 (1986).
18 C. Gadelmeier, Y. Yang, U. Glatzel, and E. P. George, Creep strength of refractory high-entropy alloy TiZrHfNbTa and comparison with Ni-base superalloy CMSX-4, Cell Rep. Phys. Sci. **3**, 100991 (2022).
19 C. J. Liu, C. Gadelmeier, S. L. Lu, J. W. Yeh, H. W. Yen, S. Gorsse, U. Glatzel, and A. C. Yeh, Tensile creep behavior of HfNbTaTiZr refractory high entropy alloy at elevated temperatures, Acta Mater. **237**, 118188 (2022).
20 G. Sahragard-Monfared, C. H. Belcher, S. Bajpai, M. Wirth, A. Devaraj, D. Apelian, E. J. Lavernia, R. O. Ritchie, A. M. Minor, J. C. Gibeling, C. Zhang, and M. Zhang, Tensile creep behavior of the Nb45Ta25Ti15Hf15 refractory high entropy alloy, Acta Mater. **272**, 119940 (2024).
21 R. L. Coble, A model for boundary diffusion controlled creep in polycrystalline materials, J. Appl. Phys. **34**, 1679 (1963).
22 F. R. N. Nabarro, Steady-state diffusional creep, Philos. Mag. **16**, 231 (1967).
23 J. Weertman, Theory of steady-state creep based on dislocation climb, J. Appl. Phys. **26**, 1213 (1955).
24 A. Srivastava, S. Gopagoni, A. Needleman, V. Seetharaman, A. Staroselsky, and R. Banerjee, Effect of specimen thickness on the creep response of a Ni-based single-crystal superalloy, Acta Mater. **60**, 5697 (2012).
25 W. Xia, X. Zhao, L. Yue, and Z. Zhang, Microstructural evolution and creep mechanisms in Ni-based single crystal superalloys: A review, J. Alloys Compd. **819**, 152954 (2020).
26 B. Xing, X. Wang, W. J. Bowman, and P. Cao, Short-range order localizing diffusion in multi-principal element alloys, Scr. Mater. **210**, 114450 (2022).
27 S. Yin, Y. Zuo, A. Abu-Odeh, H. Zheng, X. G. Li, J. Ding, S. P. Ong, M. Asta, and R. O. Ritchie, Atomistic simulations of dislocation mobility in refractory high-entropy alloys and the effect of chemical short-range order, Nat. Commun. **12**, 4873 (2021).
28 X. Liu, and W. A. Curtin, Atomistic simulations reveal strength reductions due to short-range order in alloys, Acta Mater. **263**, 119471 (2024).
29 S. Moniri, Y. Yang, J. Ding, Y. Yuan, J. Zhou, L. Yang, F. Zhu, Y. Liao,

Y. Yao, L. Hu, P. Ercius, and J. Miao, Three-dimensional atomic structure and local chemical order of medium- and high-entropy nanoalloys, Nature **624**, 564 (2023).
30 C. Kale, S. Srinivasan, B. C. Hornbuckle, R. K. Koju, K. Darling, Y. Mishin, and K. N. Solanki, An experimental and modeling investigation of tensile creep resistance of a stable nanocrystalline alloy, Acta Mater. **199**, 141 (2020).
31 B. Wang, Q. Wang, R. Luo, Q. Kan, and B. Gu, Atomistic study on high temperature creep of nanocrystalline 316L austenitic stainless steels, Acta Mech. Sin. **39**, 122470 (2023).
32 H. Yao, T. Ye, W. Yu, P. Wang, J. Wu, Y. Wu, and P. Chen, Atomic-scale investigation of creep behavior and deformation mechanism in nanocrystalline FeCrAl alloys, Mater. Des. **206**, 109766 (2021).
33 H. Yao, T. Ye, P. Wang, J. Wu, J. Zhang, and P. Chen, Structural evolution and transitions of mechanisms in creep deformation of nanocrystalline FeCrAl alloys, Nanomaterials **13**, 631 (2023).
34 G. Huang, X. Zhang, Z. Xie, W. R. Jian, R. Zhang, and X. Yao, Effects of lattice distortion and chemical short-range order on creep behavior of medium-entropy alloy CoCrNi, Mech. Mater. **177**, 104549 (2023).
35 S. Plimpton, Fast parallel algorithms for short-range molecular dynamics, J. Comput. Phys. **117**, 1 (1995).
36 R. Qiu, Y. Chen, X. Liao, Y. Lin, Y. Dou, X. He, W. Yang, W. Hu, and H. Deng, Development of a semi-empirical interatomic potential appropriate for the radiation defects in V-Ti-Ta-Nb high-entropy alloy, J. Phys.-Condens. Matter **35**, 055701 (2023).
37 P. Hirel, Atomsk: A tool for manipulating and converting atomic data files, Comput. Phys. Commun. **197**, 212 (2015).
38 W. Brostow, J. P. Dussault, and B. L. Fox, Construction of Voronoi polyhedra, J. Comput. Phys. **29**, 81 (1978).
39 E. Antillon, C. Woodward, S. I. Rao, B. Akdim, and T. A. Parthasarathy, Chemical short range order strengthening in a model FCC high entropy alloy, Acta Mater. **190**, 29 (2020).
40 J. M. Cowley, An approximate theory of order in alloys, Phys. Rev. **77**, 669 (1950).
41 S. Chen, Z. H. Aitken, S. Pattamatta, Z. Wu, Z. G. Yu, D. J. Srolovitz, P. K. Liaw, and Y. W. Zhang, Short-range ordering alters the dislocation nucleation and propagation in refractory high-entropy alloys, Mater. Today **65**, 14 (2023).
42 H. W. Yao, J. W. Qiao, M. C. Gao, J. A. Hawk, S. G. Ma, H. F. Zhou, and Y. Zhang, NbTaV-(Ti,W) refractory high-entropy alloys: Experiments and modeling, Mater. Sci. Eng.-A **674**, 203 (2016).
43 J. Bouchet, F. Bottin, G. Jomard, and G. Zérah, Melting curve of aluminum up to 300 GPa obtained through *ab initio* molecular dynamics simulations, Phys. Rev. B **80**, 094102 (2009).
44 D. Faken, and H. Jónsson, Systematic analysis of local atomic structure combined with 3D computer graphics, Comput. Mater. Sci. **2**, 279 (1994).
45 A. Stukowski, V. V. Bulatov, and A. Arsenlis, Automated identification and indexing of dislocations in crystal interfaces, Model. Simul. Mater. Sci. Eng. **20**, 085007 (2012).
46 A. Stukowski, Visualization and analysis of atomistic simulation data with OVITO—the open visualization tool, Model. Simul. Mater. Sci. Eng. **18**, 015012 (2010).
47 X. G. Li, C. Chen, H. Zheng, Y. Zuo, and S. P. Ong, Complex strengthening mechanisms in the NbMoTaW multi-principal element alloy, npj Comput. Mater. **6**, 70 (2020).
48 P. Shi, J. Yu, Z. Xie, X. Ren, X. Wu, and Y. Wang, Variation of chemical ordering induced by grain boundaries in multi-principal element alloys, Comput. Mater. Sci. **241**, 113039 (2024).
49 P. Villars, and L. D. Calvert, Pearson's Handbook of Crystallographic Data for Intermediate Phases (American Society for Metals, Metals Park, Ohio, 1985).
50 C. Li, S. Lu, S. Divinski, and L. Vitos, Theoretical and experimental grain boundary energies in body-centered cubic metals, Acta Mater. **255**, 119074 (2023).
51 X. Shen, S. Xin, S. Ding, Y. He, W. Dong, B. Sun, X. Cai, and T. Shen, Intermediate-temperature creep behaviors of an equiatomic VNbMoTaW refractory high-entropy alloy, J. Mater. Res. Tech. **24**, 4796 (2023).
52 X. Shen, B. Sun, S. Xin, S. Ding, and T. Shen, Creep in a nanocrystalline VNbMoTaW refractory high-entropy alloy, J. Mater. Sci. Tech. **187**, 221 (2024).
53 C. S. Pande, and K. P. Cooper, Nanomechanics of Hall-Petch relationship in nanocrystalline materials, Prog. Mater. Sci. **54**, 689 (2009).
54 S. G. Zaichenko, and A. M. Glezer, Disclination mechanism for plastic deformation of nanocrystalline materials, Phys. Solid State **39**, 1810 (1997).
55 J. Weertman, Steady-state creep of crystals, J. Appl. Phys. **28**, 1185 (1957).
56 A. K. Mukherjee, J. E. Bird, and J. E. Dorn, Experimental correlations for high-temperature creep, ASM-Trans. **62**, 155 (1968).
57 C. Gurney, Report of a Conference on the Strength Solids (1947), Nature **163**, 117 (1949).
58 H. Lüthy, R. A. White, and O. D. Sherby, Grain boundary sliding and deformation mechanism maps, Mater. Sci. Eng. **39**, 211 (1979).
59 R. C. Gifkins, Diffusional creep mechanisms, J. Am. Ceram. Soc. **51**, 69 (1968).
60 W. Blum, and X. H. Zeng, A simple dislocation model of deformation resistance of ultrafine-grained materials explaining Hall-Petch strengthening and enhanced strain rate sensitivity, Acta Mater. **57**, 1966 (2009).
61 S. L. Gafner, L. V. Redel, and Y. Y. Gafner, Molecular-dynamics simulation of the heat capacity for nickel and copper clusters: Shape and size effects, J. Exp. Theor. Phys. **114**, 428 (2012).

短程有序对TiVTaNb难熔高熵合金高温蠕变行为影响的原子尺度研究

张忠傲, 豆艳坤, 贺新福, 赵永鹏, 姜文佳, 杨文

摘要 蠕变是难熔高熵合金(RHEA)在高温下的一种重要力学性能. 高熵合金中短程有序(SRO)的存在及其提高合金强度或塑性的能力已被实验证实. 然而, 关于SRO与蠕变行为之间相关性的研究仍然很少. SRO影响蠕变行为的机制尚不清楚. 在本次工作中, 利用分子动力学方法模拟了TiVTaNb难熔高熵合金在不同温度和应力下的蠕变行为, 并分析了SRO对蠕变行为的影响. 结果表明, 该RHEA在能量上有利于SRO的形成. 对于多晶RHEA, 晶界能是SRO形成的重要驱动力. 值得注意的是, 在相同的加载条件下, SRO可以降低RHEA的稳态蠕变速率并改变蠕变机制. 具体而言, 具有SRO的模型将表现出较低的应力指数和晶粒尺寸指数. SRO在削弱晶界对蠕变的影响方面还发挥了重要作用. 经过分析, SRO对原子扩散的影响可以很好地解释这些现象. 此外, 通过分析不同元素的扩散能力, 发现SRO可以诱导原子扩散的局域化, 导致高应力下的应变局域化. 这项工作强调了SRO对RHEA蠕变的重要影响, 为建立合理的RHEA蠕变模型提供了参考.